Nuclear Engineering and Technology 51 (2019) 479–489

Contents lists available at ScienceDirect

Nuclear Engineering and Technology

journal homepage: www.elsevier.com/locate/net

Original Article

Comparison of oxide layers formed on the low-cycle fatigue crack surfaces of Alloy 690 and 316 SS tested in a simulated PWR environment

Junjie Chen [a], Andrieanto Nurrochman [a], Jong-Dae Hong [b], Tae Soon Kim [c], Changheui Jang [a, *], Yongsun Yi [d]

[a] Korea Advanced Institute of Science and Technology, 34141, Daejeon, Republic of Korea
[b] Korea Atomic Energy Research Institute, 34057, Daejeon, Republic of Korea
[c] Central Research Institute, Korea Hydro and Nuclear Power Co., Ltd., 34101, Daejeon, Republic of Korea
[d] Khalifa University, Abu Dhabi, United Arab Emirates

ARTICLE INFO

Article history:
Received 7 June 2018
Received in revised form
19 September 2018
Accepted 8 October 2018
Available online 8 October 2018

Keywords:
Environmentally-assisted fatigue
Alloy 690
316 SS
Oxide layer
Electrochemical analysis

ABSTRACT

Low-cycle fatigue (LCF) tests were performed for Alloy 690 and 316 SS in a simulated pressurized water reactor (PWR) environment. Alloy 690 showed about twice longer LCF life than 316 SS at the test condition of 0.4% amplitude at strain rate of 0.004%/s. Observation of the oxide layers formed on the fatigue crack surface showed that Cr and Ni rich oxide was formed for Alloy 690, while Fe and Cr rich oxide for 316 SS as an inner layer. Electrochemical analysis revealed that the oxide layers formed on the LCF crack surface of Alloy 690 had higher impedance and less defect density than those of 316 SS, which resulted in longer LCF life of Alloy 690 than 316 SS in a simulated PWR environment.

1. Introduction

Degradation of structural materials used in the primary coolant system of the pressurized water reactor (PWR) can be significantly enhanced in a corrosive coolant environment at temperatures ranging from 270 °C to 345 °C [1,2]. For example, the low cycle fatigue (LCF) damage of metallic components in the primary coolant environment was known to be considerably greater than that in an air environment. This phenomenon was called environmentally-assisted fatigue (EAF) and considered as one of the key degradation mechanisms in PWR [3–5]. Over the years, extensive tests have been performed worldwide and the results were incorporated into a report, NUREG/CR-6909, which contains comprehensive EAF test data of several structural metals including stainless steels (SSs) and Ni–Cr–Fe alloys [4]. Afterwards, a regulatory guide, Reg. Guide 1.207, was issued by the U.S. nuclear regulator to specifically address the EAF issue in the design and construction of key components of nuclear power plants [6].

Recently, LCF tests of 316LN, an austenitic SS, and Alloy 690, Ni–Fe–Cr alloys, in a simulated PWR environment have been performed and the results were analyzed to understand the applicable EAF mechanisms [7–9]. In those studies, based on the detailed microstructure and fatigue crack surface analysis on the specimens tested in a PWR environment, the hydrogen-induced cracking (HIC) mechanism was proposed as the dominant factor in the fatigue life reduction for austenitic SSs and Ni–Fe–Cr alloys. Additionally, corrosion at the crack tip was considered to be the major source of hydrogen available to be absorbed into the crack tip region, which then would promote HIC. Thus, better EAF resistance of Alloy 690 than 316LN was attributed to the superior corrosion resistance of the former [9]. In addition, the different corrosion resistance of Alloy 690 and 316LN at the crack tip would result in oxide layer with different characteristics, which can be correlated with their EAF behavior. Meanwhile, extensive studies have been performed to reveal the mechanism of stress corrosion crack (SCC) propagation through the characterization of the oxides on the SCC crack

* Corresponding author.
E-mail addresses: junjiechen@kaist.ac.kr (J. Chen), andrienurr@kaist.ac.kr (A. Nurrochman), jongd@kaeri.re.kr (J.-D. Hong), taesoon.kim@khnp.co.kr (T.S. Kim), chjang@kaist.ac.kr (C. Jang), yongsun.yi@kustar.ac.ae (Y. Yi).

https://doi.org/10.1016/j.net.2018.10.007

Table 1
Chemical compositions of Alloy 690 and 316 SS analyzed by ICP (wt %).

	C	Ni	Cr	Fe	Si	Mn	P	S	Al	Cu	Ti	Mo	Co
Alloy 690	0.01	59.31	29.76	9.30	0.39	0.21	0.003	0.001	0.36	–	0.26	–	0.16
316 SS	0.05	10.73	17.34	67.9	0.60	0.64	0.020	0.005	–	0.25	–	2.15	–

surface [10,11]. The roles of dissolution and oxidation were deduced from the oxide layers characteristics, then cracking mechanisms were proposed based on the results. However, oxide layers on the fatigue crack surface have rarely been the focus of study on EAF behavior of austenitic alloys.

In this study, to better understand the EAF behavior of austenitic alloys, such as 316 SS and Alloy 690, LCF tests were performed, and oxide layers on the fatigue crack surface were characterized. Electrochemical techniques, such as electrochemical impedance spectroscopy (EIS) and Mott-Schottky (M-S) analysis, were utilized to investigate the oxide layers at the crack tip and mouth region of the fatigue crack surface. In addition, various analytical techniques were used to observe the microstructure and composition of oxide layers. The results were then discussed in view of the different EAF resistance of 316 SS and Alloy 690.

2. Materials and experiment

2.1. Materials and LCF tests

The test materials used in this study were Alloy 690 and 316 SS. The chemical composition analyzed by the inductively coupled plasma (ICP) method is listed in Table 1. The test specimens were machined from the annealed plates into round-bar shapes with a gauge length and diameter of 19.05 mm and 9.63 mm, respectively, to be consistent with the previous studies [5,7–9]. The LCF tests were performed according to ASTM E-606 in strain control mode with a fully reversed triangular waveform at 310 °C in simulated PWR water as summarized in Table 2. The system pressure was maintained at 15 MPa. The strain rate was 0.004%/s, and the strain amplitude was 0.4%. During the test, the dissolved oxygen (DO) and dissolved hydrogen (DH) concentrations were kept under 5 ppb and approximately at 25 cc/kg-H_2O, respectively. Additionally, the conductivity was maintained at 20–25 μS/cm during the test. The LCF tests were stopped when the tensile peak stress decreased by 25% from the maximum values, and the corresponding number of cycles was recorded as fatigue life. Then, specimens were broken open and sectioned for subsequent microstructure observation and electrochemical analysis.

2.2. Electrochemical measurements

The electrochemical measurements were performed at the crack tip and mouth regions of the LCF tested specimens as shown schematically in Fig. 1. The specimens for electrochemical measurements were taken at the fatigue crack surface of the LCF tested specimens of Alloy 690 and 316 SS. The specimens were then masked with silicon sealant, leaving only the exposed areas of a few mm^2 at the 'crack tip' and 'mouth' regions of the fatigue crack surface as shown in Fig. 1. The location of the exposed area was maintained as close as possible to the intended locations, such that exposed area of the 'crack tip' and 'mouth' regions was kept within 0.5–1.0 mm from the fatigue crack tip and the outer surface, respectively. The intention was that, by placing the exposed area of the 'crack tip' region as close as possible to the real fatigue crack tip, the characteristics of oxides formed at the real fatigue crack tip could be approximately obtained by analyzing the 'crack tip' region.

Then, for both the crack tip and mouth regions, the electrochemical impedance spectroscopy (EIS) analysis was performed at open circuit state in a borate buffer solution (H_3BO_3 (0.05 M) + $Na_2B_4O_7.10H_2O$ (0.075 M) at pH 9.2) at ambient temperature using a GAMRY electrochemical workstation (Reference 3000™). A conventional three-electrode system with a saturated calomel electrode (SCE) as a reference electrode was used. The amplitude of the AC signal was 10 mV within the frequency range from 100 kHz to 1 Hz. The oxygen content in the test solution was minimized by continuously purging the system with argon gas during the test. A Mott-Schottky (M-S) analysis was carried out in the same buffer solution used for EIS analysis. The potential was scanned in the anodic direction from −0.6 V(SCE) to 0.6 V(SCE) at a scan rate of 50 mV/s. The capacitance measurements were conducted in a single frequency of 1000 Hz with 10 mV AC amplitude.

2.3. Oxide layers and fracture surface observation

The structure and crystallographic details of the oxide layer were observed by using transmission electron microscopy (TEM, FEI-Tecnai™ G2 F30) at an accelerating voltage of 300 kV. The TEM analyses were performed on the samples taken at the crack tip and mouth regions of the LCF specimens tested at 310 °C in simulated PWR

Table 2
Low cycle test fatigue conditions in a simulated PWR environment.

Test materials	Alloy 690, 316 SS
Condition	PWR water (310 °C)
Wave	Fully reversed triangle waveform (R = -1)
Strain rate (%/s)	0.004%/s
Strain amplitude (%)	0.4%
DO/DH	<5 ppb/2.2 ppm (~25 cc H_2/kg-H_2O)
Conductivity at RT	20-25 μS/cm (1200 ppm H_3BO_3 + 2.2 ppm LiOH)
pH at RT	6–7

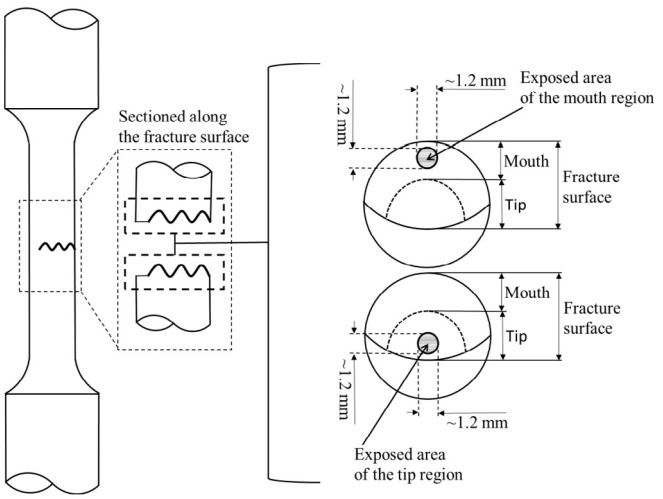

Fig. 1. Schematic diagram of specimen preparation for the electrochemical measurements taken from the LCF tested specimens of Alloy 690 and 316 SS. Exposed areas at the crack tip and mouth regions are indicated.

water. The thin foil TEM samples were prepared using a focus ion beam (FIB, FEI-Helios™ NanoLab 450 F1). TEM images and diffraction patterns were obtained on the TEM specimens containing the cross-section of the fatigue crack. Scanning transmission electron microscopy (STEM) line scanning analysis was also conducted to obtain compositions of the oxide layers through the thickness. For fracture surface observation, a field emission scanning electron microscope (FE-SEM, FEI-Magellan 400) was used.

3. Results and discussion

3.1. LCF life and fatigue crack surface observations

The LCF life test results of Alloy 690 and 316 SS in a simulated PWR primary water environment are shown in Fig. 2. Also shown are the LCF life test results in air environment and LCF life curve calculated using the equation in the NUREG/CR-6909 [4]. As shown in the figure, both materials show shorter LCF life in the simulated PWR water than in air. The longer LCF life and consequently less environmental effect for Alloy 690 than 316 SS are consistent with previous reports by authors [5,9] and other researchers [3,4,12,13]. For comparison, one representative specimen from each material tested at the same condition was chosen for further analysis. That is, an LCF tested Alloy 690 specimen with a fatigue life of 5012 cycles (corresponding to approximately 556 h of test time) and an LCF tested 316 SS specimen with a fatigue life of 2715 cycles (corresponding to approximately 301 h of test time) were selected.

The fatigue crack surface at the crack tip region of each specimen was observed under SEM and the results are shown in Fig. 3 along with the chemical composition of surface oxides analyzed by EDS. The crack tip regions of the fatigue crack surface of the 316 SS and Alloy 690 are thought to contain the relatively newly formed oxides during the fatigue crack growth while the environmental effects are active. The SEM micrographs of the fatigue crack surfaces at the crack tip region of Alloy 690 and 316 SS are presented in Fig. 3a and b, respectively. The difference in oxide morphology on fatigue crack surfaces are evident such that large granular type oxides are covering the crack surface of 316 SS, while the fatigue crack surface of Alloy 690 is mostly free of granular type oxides. The chemical compositions of the oxides on the fatigue crack surface were analyzed by EDS at three positions in the SEM micrographs and the results are shown in Fig. 3. Though not quantitatively accurate, the EDS results qualitatively show the oxides on Alloy 690 are enriched with Cr (the Cr/Ni ratio is greater than that in the matrix of Alloy 690), while those on 316 SS are enriched with Fe

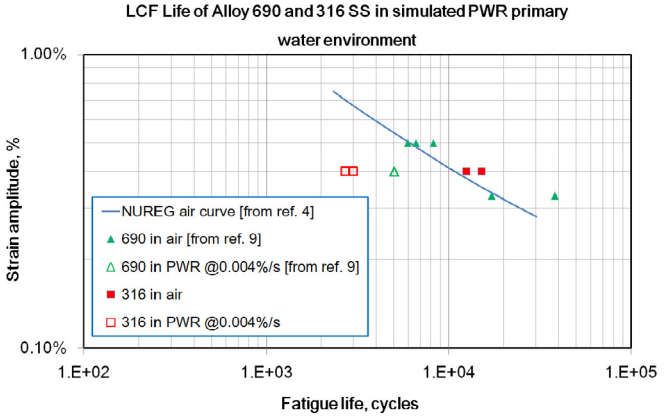

Fig. 2. LCF life test results of Alloy 690 and 316 SS in a simulated PWR primary water environment. Also shown are the LCF life test results in air environment and LCF life curve estimated from the NUREG/CR-6909 [4] for comparison.

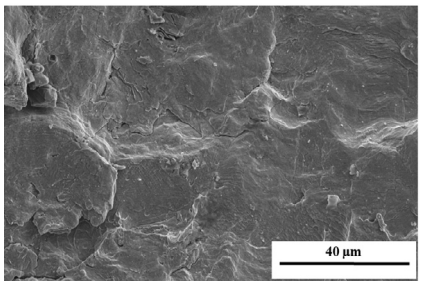

a)

EDS measurements of Alloy 690 fracture surface

Element	Wt %
O	3.44±0.90
Fe	0
Ni	39.96±3.12
Cr	56.61±4.03

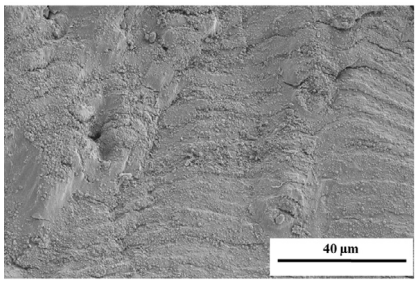

b)

EDS measurements of 316 SS fracture surface

Element	Wt %
O	28.25±2.39
Fe	51.1±6.06
Ni	11.38±6.81
Cr	9.28±1.62

Fig. 3. SEM Fracture surface micrographs and EDS analysis results of a) Alloy 690 and b) 316 SS at the crack tip region.

with less Cr. In addition, striations are clearly observed on the fatigue crack surface of 316 SS while they are less clear on Alloy 690. As the striations are associated with crack tip blunting during fatigue crack growth and considered as an evidence of metal dissolution [7,8], the relatively weak and narrow striation on the fatigue crack surface of Alloy 690 could indicate the lower environmental effect in the crack tip region. The lower oxygen concentration for Alloy 690 could be the result of the very thin oxide layer on the fatigue crack surface, which also indicates the better corrosion resistance of Alloy 690 [9].

Previously, Cunha Belo et al. [14] reported that the composition of the outer oxide layer formed on 316L SS immersed in a PWR environment for 2000 h would be $Ni_{0.75}Fe_{2.25}O_4$. Meanwhile, Soulas et al. [15] reported that the outer oxide layer on 316L SS would be AB_2O_4 type spinel after a short exposure time of several minutes, but it would be Fe_3O_4 crystallites after longer exposure time (>5 h). Therefore, based on the EDS results and relatively short exposure time to the PWR environment, the outer oxides that formed on the 316 SS fatigue crack surface are considered to be the mixture of Fe-rich spinel and Fe_3O_4.

Meanwhile, for Alloy 690, there have been some studies on the oxide formed in a PWR environment [16–18]. Many studies on Alloy 690 reported that the oxide layers consisted of duplex structures with large Fe-rich oxide crystallites at the outer layer and continuous Cr-rich oxides at the inner layer. For example, Sennour et al. [18] reported that the $Ni_{(1-z)}Fe_{(2+z)}O_4$ crystallites were found at the outer part of the oxide layers on Alloy 690 exposed for 66 h and 858 h in a simulated PWR environment. Meanwhile, Lefaix-Jeuland et al. [19] reported the formation of a continuous nickel iron chromate ($Ni_{(1-x)}Fe_xCr_2O_4$) layer on top of Cr_2O_3 granules without the presence of large Fe-rich crystallites at the outer layer after exposure for 304 h in a simulated PWR environment using Alloy 690 with a hardened surface state with a number of defects [19]. As crack tip blunting proceeds the fatigue crack growth in a simulated PWR environment [9], the exposed surface of the fatigue crack would be at a hardened state with a number of defects. Therefore, the oxides formed on fatigue crack surface of Alloy 690 (Fig. 3a) would be close

to those reported by Lefaix-Jeuland et al. [19]. However, considering the absence of Fe from the EDS analysis result, it is likely that the oxides are nickel chromite ($NiCr_2O_4$) proposed by Beverskog and Puigdomenech [20] and Marchetti et al. [21] based on a Pourbaix diagram and XPS analysis results, respectively.

3.2. TEM analysis of oxide layers

Fig. 4 shows the cross-section TEM analysis results of the fatigue crack surface of Alloy 690 containing oxide layers at the crack tip and mouth regions of the LCF crack. EDS line scanning analyses were performed on the LCF crack surface of Alloy 690 and the results are also shown in Fig. 4. As shown in the figure, the oxides formed at the mouth region are much thicker (100–300 nm) than those at the crack tip region (50–70 nm), which is expected considering that the mouth region is exposed to PWR water for much longer than the crack tip region. It seems that, at the mouth region, outer layer with small amount of Fe is present on top of the inner layer rich in Cr and Ni. Meanwhile, at the mouth region, the inner layer is well developed but the presence of outer layer is not

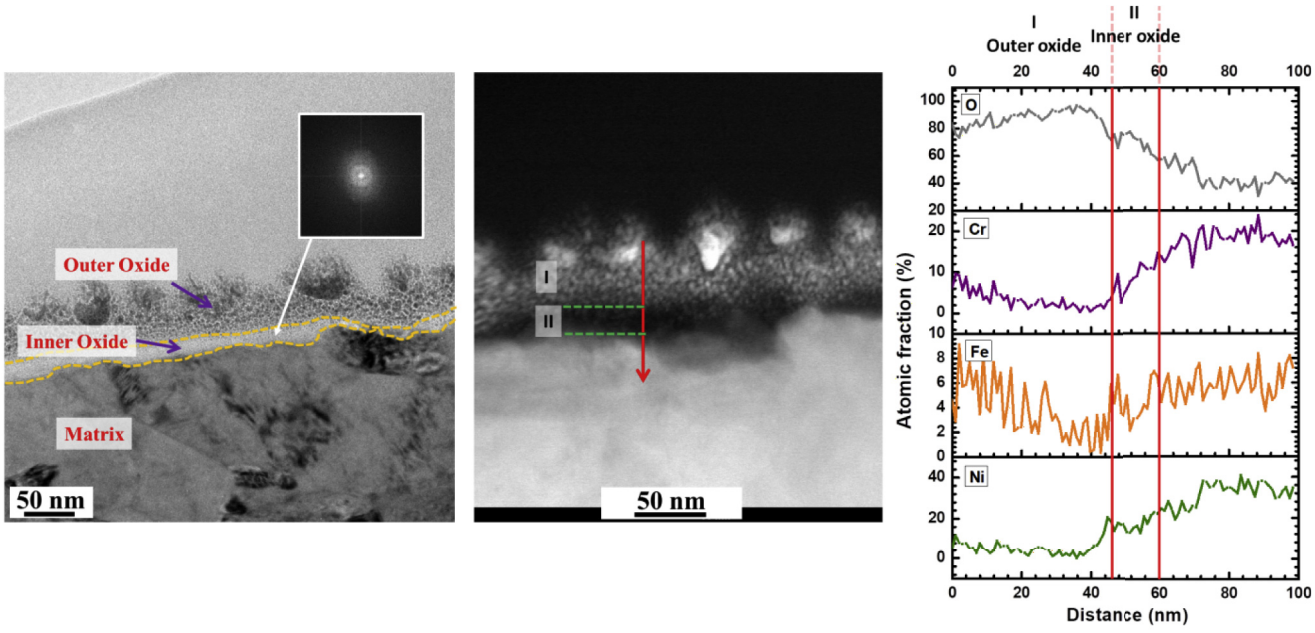

a)

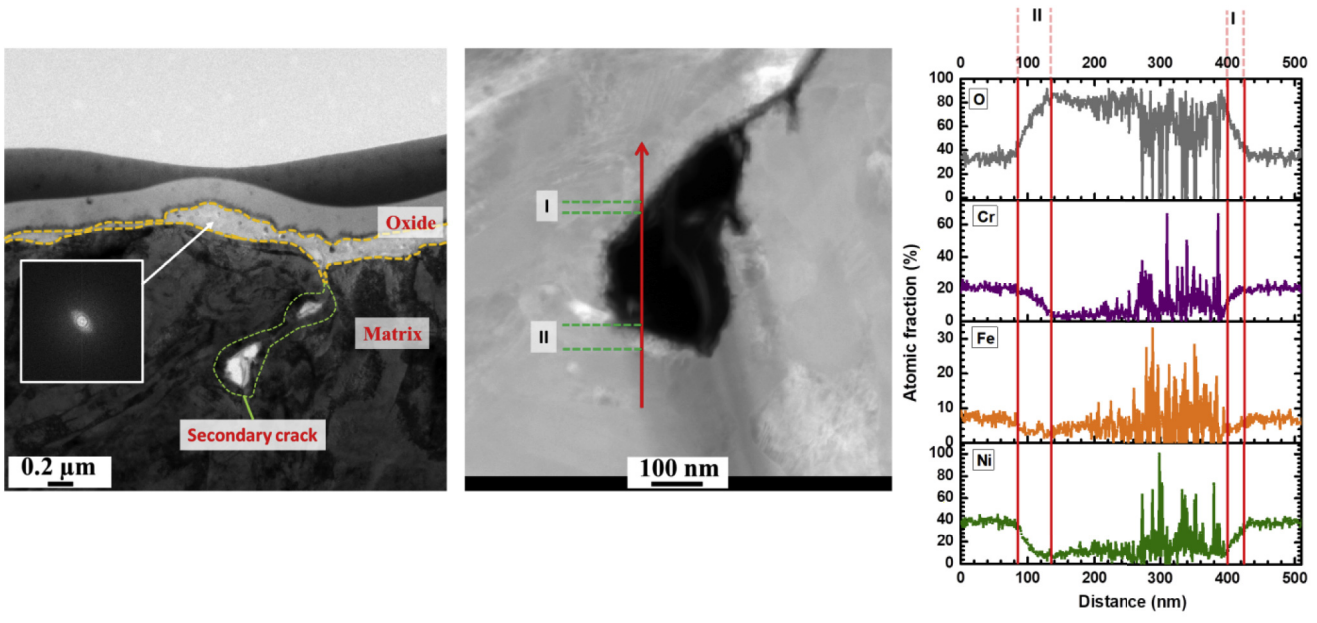

b)

Fig. 4. Cross-section TEM analyses (HRTEM image analysis, diffraction analysis, STEM EDS line scanning analysis) of LCF tested Alloy 690 (a) at the crack tip and (b) the mouth regions of the LCF crack, respectively. The dashed line indicates the oxide films formed on the LCF crack surface.

clear. The EDS line scanning results show that Cr and Ni are dominant while Fe is mostly absent in the oxide layer at the mouth region. Therefore, nickel chromite ($NiCr_2O_4$) would be the probable oxide formed on the fatigue crack surface of Alloy 690, which is consistent with the results of previous studies [20,21]. Interestingly, TEM diffraction analysis shows that the oxide layers are mostly an amorphous structure at both regions. This is rather surprising as the presence of crystalline Cr-rich oxides on Alloy 690 exposed to PWR water have been well reported by other researchers [18,19].

Fig. 5 shows the cross-section TEM analysis results of the fatigue crack surface of 316 SS containing oxide layers at the crack tip and mouth regions of the LCF crack. TEM observations on 316 SS oxide reveal similar oxide layer morphology (thin inner layer and large outer nodules) at both the crack tip and mouth regions. The inner layer is somewhat thinner at the crack tip region (30–100 nm) compared to that at the mouth region (150–200 nm). Nonetheless, the overall thickness of oxide layer is much greater than that of Alloy 690 (Fig. 4). Unlike Alloy 690, crystalline diffraction patterns are clearly detected for both the inner oxide layer and the large outer oxide nodules. The STEM line scanning analysis results show that the large outer oxide nodules are rich in Fe. Considering the diffraction patterns, the outer oxide nodules would be as Fe_3O_4 crystallites at both the crack tip and mouth regions of the LCF crack. Meanwhile, inner oxide layers are rich in Fe and Cr with small amount of Ni at both the crack tip and mouth regions of the LCF crack. The composition of the inner oxide layer formed on 316 SS have been proposed as Cr_2O_3 and (Fe, Ni)Cr_2O_4 by several authors [14,15]. Considering that considerable amount of Fe is present at the inner oxide layer, the inner oxide layer would be (Fe,Ni)Cr_2O_4.

The investigation of oxide structure on the fatigue crack surface

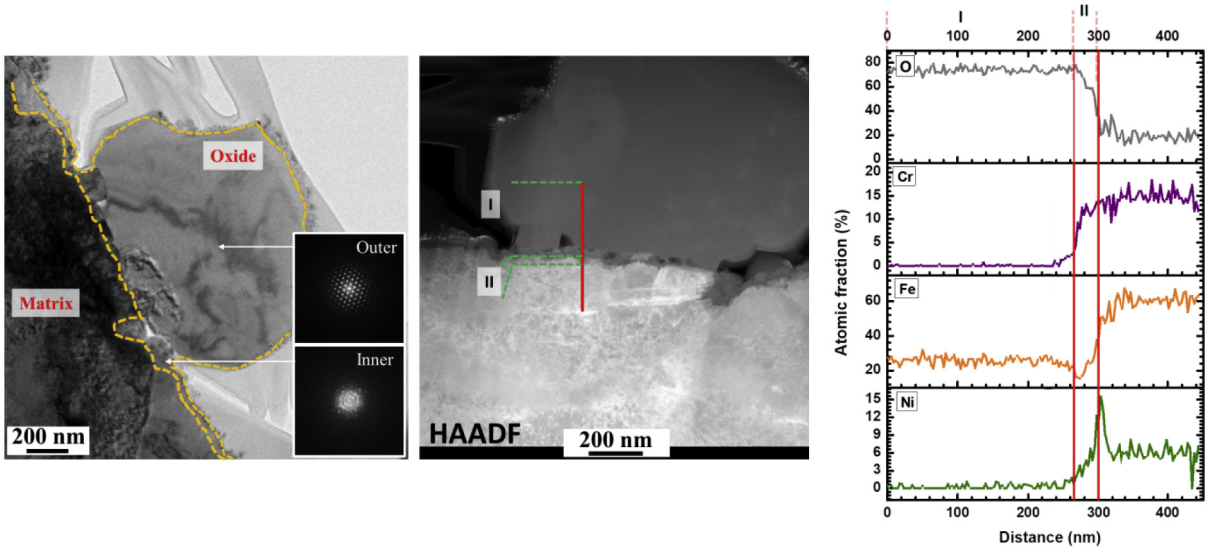

a)

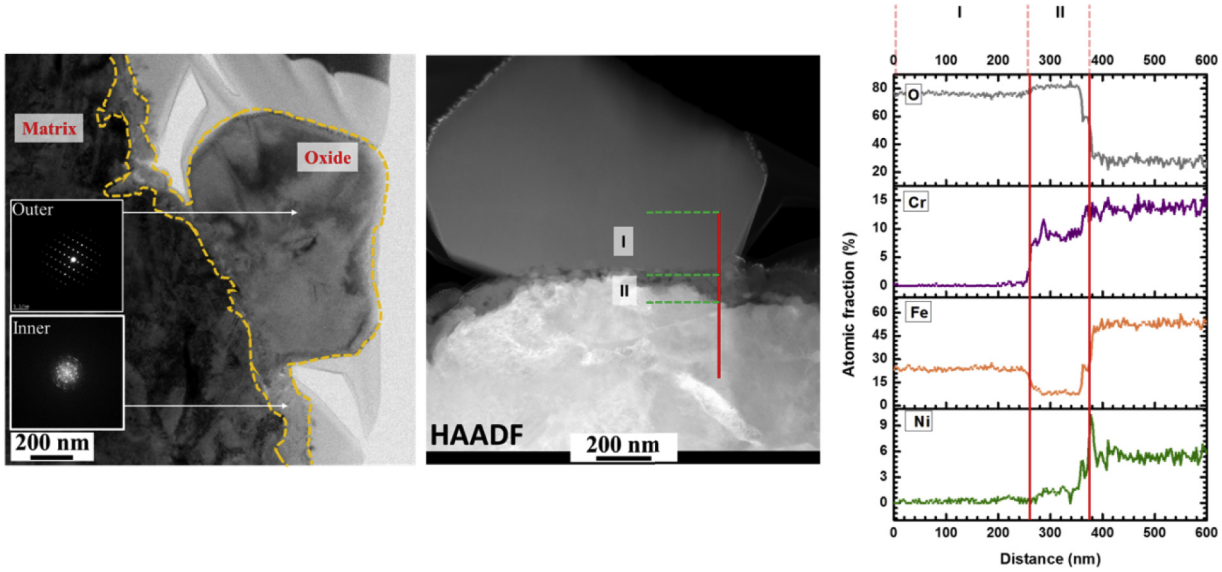

b)

Fig. 5. Cross section TEM analyses (HRTEM image analysis, diffraction analysis, STEM EDS line scanning analysis) of LCF tested 316 SS (a) at the crack tip and (b) mouth regions of the LCF crack, respectively. The dashed line indicates the oxide films formed on the LCF crack surface.

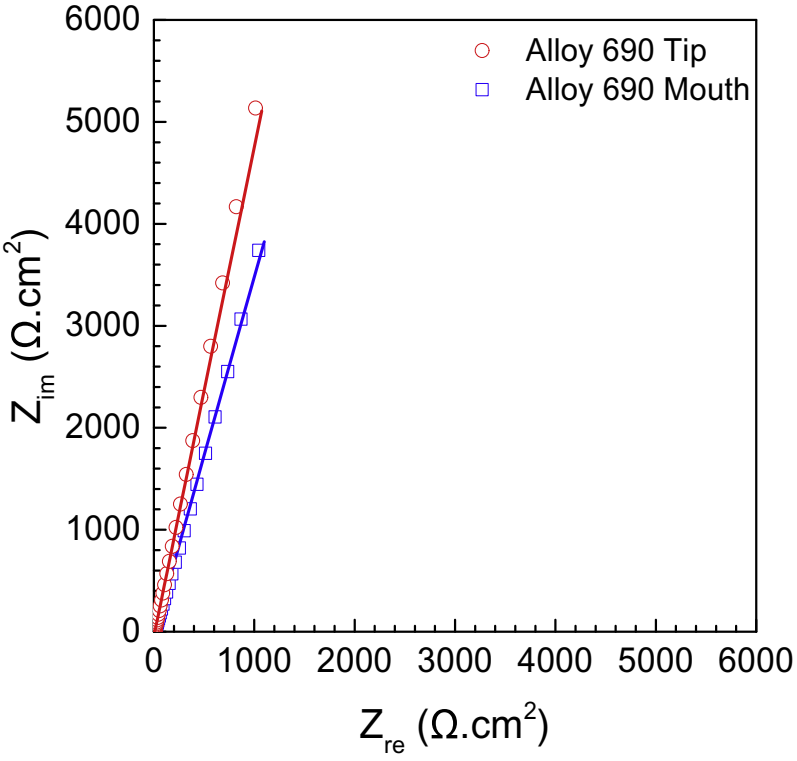
Alloy 690 Tip
Alloy 690 Mouth
Z_{im} ($\Omega.cm^2$)
Z_{re} ($\Omega.cm^2$)
0
1000
2000
3000
4000
5000
6000

a)

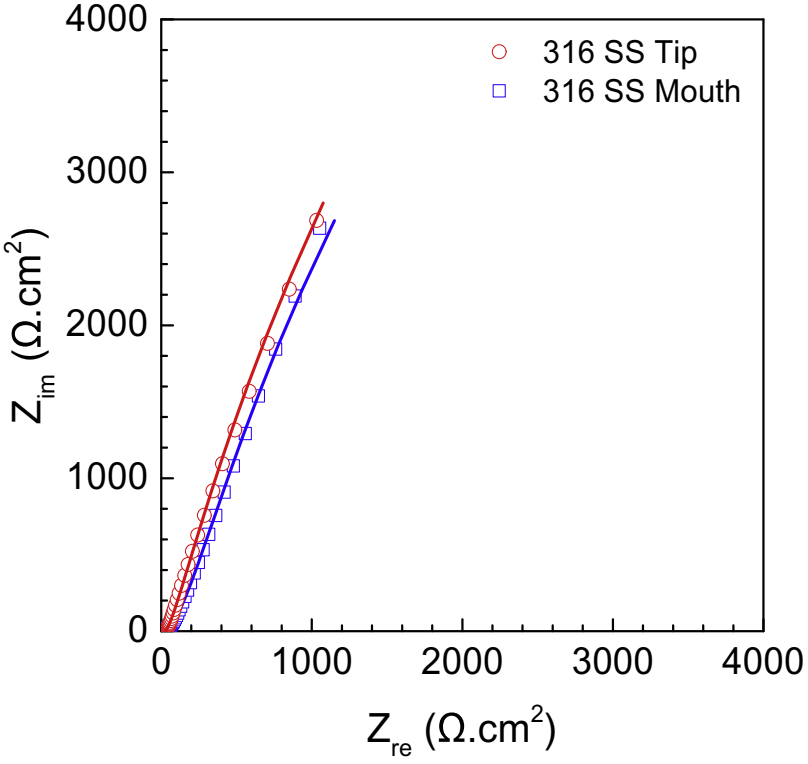
316 SS Tip
316 SS Mouth
Z_{im} ($\Omega.cm^2$)
Z_{re} ($\Omega.cm^2$)
0
1000
2000
3000
4000

b)

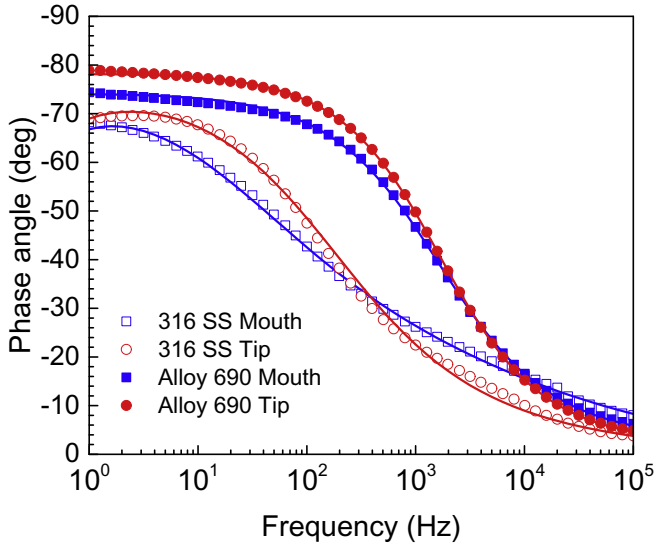

a)

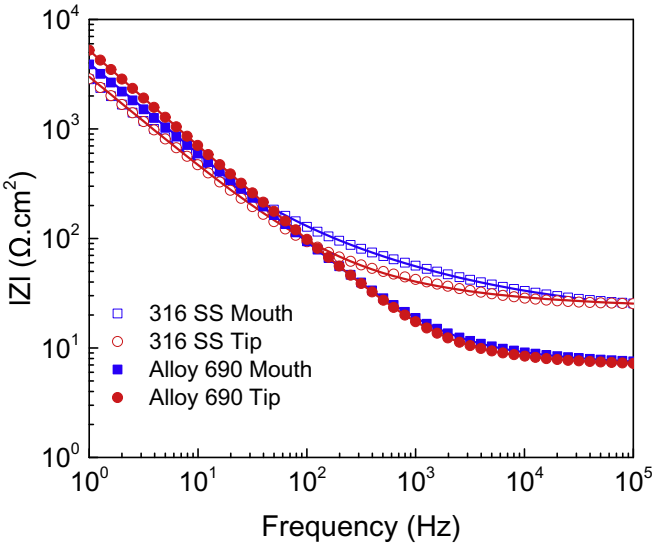

b)

Fig. 7. Impedance spectra (Bode plots) of oxide films formed at the crack tip and mouth regions of Alloy 690 and 316 SS LCF crack surface: (a) phase angle vs. log f curves and (b) log |Z| vs. log f curves. The lines are fitting results. (in a Borate buffer solution at room temperature).

of Alloy 690 and 316 SS showed that the thin Cr-rich oxide layer is formed on top of the matrix, which would provide protection from further corrosion in a PWR environment. The protectiveness of this oxide layer may influence the environmental fatigue resistance of each material during an LCF test, where environmental effects are dominantly felt at the region near the growing fatigue crack tip. During the cyclic loading, if the stress is sufficient, the oxide layers at the crack tip would be broken and lose protectiveness against corrosion. However, subsequent formation of oxide layers on the

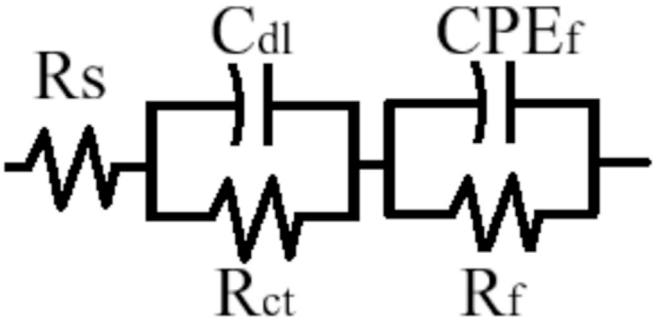

Fig. 8. Equivalent electrical circuit model employed to simulate measured impedance data. Where, R_S is the solution resistance; R_{ct} is the charge-transfer resistance of the Faraday processes; C_{dl} is used as the capacitance of electric double layer; R_f represents the resistance for the oxide film and CPE_f is the constant phase element for the oxide film.

exposed metal surface would provide the re-passivation of the metal surface at the crack tip region. If the oxide layers are sufficiently protective, the further dissolution of metal could be prevented, and the thickness of the oxide layer could be minimized. According to STEM/EDS analysis shown in Figs. 4 and 5, the inner oxide layers formed at the crack tip region are rich in Cr and Ni for Alloy 690 and Cr and Fe for 316 SS, respectively, while its thickness is somewhat greater for 316 SS compared to Alloy 690. Meanwhile, Alloy 690 (with thinner inner oxide layer) showed about twice longer LCF life than 316 SS (with thicker oxide layer) as shown in Fig. 2. Therefore, the thickness of inner Cr-rich oxide layer at the crack tip region could not be correlated with the LCF life in a simulated PWR environment.

3.3. EIS analysis of oxide layers

Prior to the EIS measurements, the specimens were immersed for 1 h in the buffer solution purged with argon gas, then the open-circuit potential (OCP) was measured. For Alloy 690, the measured OCP values were −0.098 V(SCE) and −0.115 V(SCE) for the specimens taken at the mouth and crack tip regions, respectively. Meanwhile, for 316 SS, the OCP values were −0.137 V(SCE) and −0.334 V(SCE) for the specimens taken at the mouth and crack tip regions, respectively. The EIS measurements were then conducted at OCP.

Fig. 6 and Fig. 7 show the EIS spectra measured for the oxide layers on the fatigue crack surfaces of the LCF tested Alloy 690 and 316 SS. The validity of the results is verified with the Kramers-Kronig transformation (KKT) to check the linearity, causality and stability of system [22]. In this study, the KKT results are in perfect match with the experimental results (not shown here), which confirmed that the requisite conditions are satisfied and the EIS results are considered valid. The Nyquist plots shown in Fig. 6 reveal that the radius of capacitance loops of oxide films formed on the LCF crack surface of Alloy 690 are greater than those of 316 SS. Also, for Alloy 690 and 316 SS, the radius of capacitance loops of oxide films at the mouth regions are lower than in the crack tip regions.

It has been known that, in the Bode plots, a high-frequency region in EIS diagrams would mainly reflect the electrochemical characteristics of the oxide film and the lower-frequency region would reflect the characteristics of the electric double layer and Faraday processes [23]. According to the Bode plots of oxide films

Fig. 6. Impedance spectra (Nyquist plots) of oxide films formed at the crack tip and mouth regions of (a) Alloy 690 and (b) 316 SS LCF crack surface. The lines are fitting results. (in a Borate buffer solution at room temperature).

Table 3
Calculated of fitting parameters for the electrical circuit model of oxide layer in Fig. 8.

Materials	Location	R_s ($\Omega.cm^2$)	R_{ct} ($10^4\ \Omega\ cm^2$)	C_{dl} ($10^{-5}S\ s^n/cm^2$)	R_f ($10^3\ \Omega\ cm^2$)	CPE_f ($10^{-3}S\ s^n/cm^2$)
Alloy 690	Crack Tip	6.00	177	3.87	5.11	64.8
	Mouth	5.50	111	5.51	5.41	60.6
316 SS	Crack Tip	23.0	2.39	7.13	15.3	2.04
	Mouth	19.4	2.19	7.28	19.9	1.12

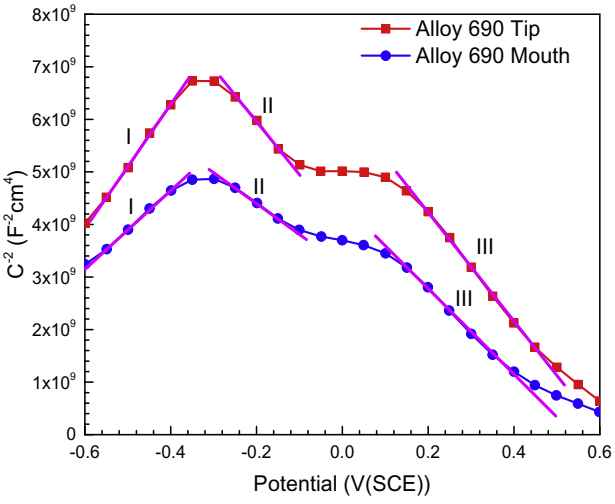

a)

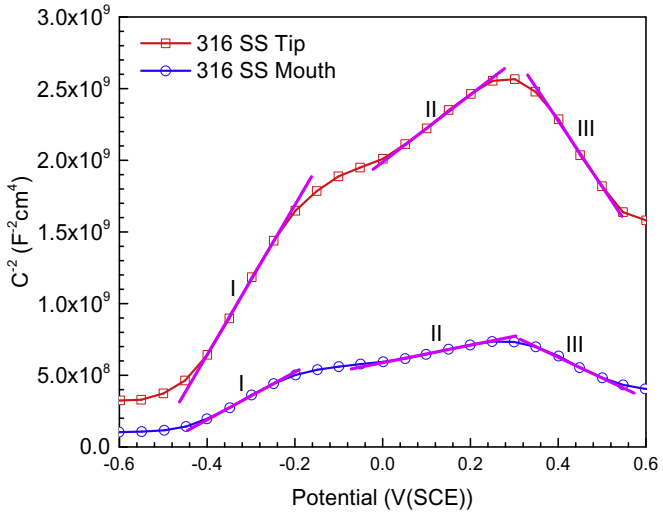

b)

Fig. 9. Mott-Schottky plots of oxide films formed at the crack tip and mouth regions of the LCF crack surface of (a) Alloy 690 and (b) 316 SS (obtained in Borate buffer solution at room temperature).

formed on the LCF crack surfaces of Alloy 690 and 316 SS, the phase angles of the mouth region are lower than the crack tip region in high frequency range, and this difference is more obvious for 316 SS, as shown in Fig. 7a. The resistance values at the mouth regions are higher than those at the crack tip regions, as shown in Fig. 7b. It reveals that the oxide films form at the mouth regions with lower film capacitance and higher resistance values, indicating the oxide films in the mouth regions being thicker. The resistance values in high frequency range of Alloy 690 being lower than 316 SS indicates that thinner oxide films formed on the LCF crack surface of Alloy 690 than 316 SS. These are in good agreement with the cross section TEM observation of oxide films shown in Figs. 4 and 5. According to Fig. 7, in the medium-low frequency range of Bode plots, the phase angles at the mouth regions are higher than those at the crack tip regions, and the resistance values of the mouth region are lower than the tip region for Alloy 690. The difference of resistance values between the mouth and crack tip regions are not obvious for 316 SS in the medium-low frequency range of Bode curves. These results reflect that the oxide films formed on the crack tip regions have higher reaction resistance than the mouth regions. Lower phase angles and higher resistance of Alloy 690 in medium-low frequency range of Bode curves indicate the oxide films of Alloy 690 have higher reaction resistance than 316 SS.

An electrical circuit model, shown in Fig. 8, is utilized to quantitatively extract the charge carriers transport parameters. The fitting results are listed in Table 3. The fitting results clearly show that the values of R_f for oxide films formed at the mouth regions are higher than those at the crack tip region, and the CPE_f are lower at the mouth region for both Alloy 690 and 316 SS, which means the thicker oxide films exist at the mouth regions. The reaction resistances of oxide films at the mouth regions are lower because of the lower R_{ct} and higher C_{dl}. The oxide films of Alloy 690 are thinner than 316 SS but have higher reaction resistance due to the lower R_f and C_{dl} and higher CPE_f and R_{ct}. These results agree well with the deduction from Bode plots.

Meanwhile, surface-active agents such as hydrogen can diffuse through the oxide layers and be absorbed into the metal [24,25]. This may be accompanied by embrittlement and reduced fatigue life. The transport behavior of hydrogen through oxide layers is influenced by the resistance of charge carrier movement including point defects such as vacancies and ions. Correspondingly, due to lower resistance against charge carrier movement, 316 SS may have a higher susceptibility to experiencing HIC resulting in reduced fatigue life.

3.4. Mott-Schottky analysis of oxide layers

The Mott-Schottky (M-S) analysis provides semiconducting

Table 4
Defect densities of oxide layers formed on the LCF crack surface at the crack tip and mouth regions of Alloy 690.

		Region I, N_D ($10^{20}\ cm^{-3}$)	Region II, N_A ($10^{20}\ cm^{-3}$)	Region III, N_A ($10^{20}\ cm^{-3}$)
Alloy 690	Crack Tip	5.96	10.8	10.1
	Mouth	9.42	18.2	12.6

Table 5
Defect densities of oxide layers formed on the LCF crack surface at the crack tip and mouth regions of 316 SS

		Region I, N_D (10^{20} cm^{-3})	Region II, N_D (10^{20} cm^{-3})	Region III, N_A (10^{20} cm^{-3})
316 SS	Crack Tip	13.3	31.7	24.1
	Mouth	43.2	12.0	73.3

properties by measuring the capacitance in the space charge layer or the depletion region as a function of the applied potential [17,26,27]. The relationship of the capacitance in the space charge layer (C_{SC}^2) with the potential (U) is expressed through the following Mott-Schottky equations:

$$\frac{1}{C_{SC}^2} = \left(\frac{2}{\varepsilon\varepsilon_0 e N_D}\right)\left(U - U_{FB} - \frac{kT}{e}\right) \text{ for the n – type semiconductor} \quad (1)$$

$$\frac{1}{C_{SC}^2} = -\left(\frac{2}{\varepsilon\varepsilon_0 e N_A}\right)\left(U - U_{FB} + \frac{kT}{e}\right) \text{ for the p – type semiconductor} \quad (2)$$

In above equations, the densities of charge carriers, such as the acceptor and donor, are N_A and N_D, respectively. ε is the dielectric constant of the oxides, ε_0 is the vacuum permittivity, e is the electron charge, k is the Boltzmann constant, T is the absolute temperature, U is the applied potential, and U_{FB} is the flat band potential. For an n-type semiconductor, the donor species or the oxygen vacancy ($V_o^{\cdot\cdot}$) and cation interstitial (M_M) are the dominant charge carriers in the oxide layers. The cation vacancy ($V_M^{X^-}$) is the charge carrier for a p-type semiconductor.

Fig. 9 shows the C-2 SC vs. potential plots measured for the surface oxides formed at the crack tip and mouth regions of the LCF crack surface of 316 SS and Alloys 690. The calculated defect densities on the basis of equations (1) and (2) are presented in Tables 4 and 5. The plots of the M-S relationship for Alloy 690 exhibit positive slope at the potential of −0.6 V(SCE) up to around −0.3 V(SCE) (region I), indicating the characteristic of n-type semiconductor. Negative slopes are shown at the potential from around −0.3 V(SCE) to −0.1 V(SCE) (region II) and from around 0.1 V(SCE) to 0.5 V(SCE) (region III), indicating the feature of p-type semiconductor. These results suggest that the oxide layers behave similar to p-n heterojunction semiconductors. The measured C-2 SC of oxide film formed at the mouth region of Alloy 690 is lower than that at the crack tip region in the whole potential scale. According to the calculated point defect densities shown in Table 4, the N_D and total N_A (N_A in region II and region III) at the mouth region are higher than those at the crack tip region, indicating the point defect densities at the mouth region are higher than those at the crack tip region.

For the oxide layers formed on 316 SS, the M-S plots showed p-n heterojunction semiconductors feature at the crack tip and mouth regions. The plots present positive slope at the potential ranges from around −0.5 V(SCE) to −0.2 V(SCE) (region I) and from around 0 V(SCE) to 0.25 V(SCE) (region II), which exhibit the n-type semiconductor behavior. The slope subsequently becomes negative at the potential range from around −0.3 V(SCE) to 0.55 V(SCE) (region III), showing the p-type semiconductor behavior. The measured C-2 SC of oxide film formed at the mouth region of 316 SS is much lower than that at the crack tip region in the whole potential scale. The calculated point defect densities shown in Table 5 reveals that the total N_D (N_D in region I and region II) and N_A at the mouth region are higher than those at the crack tip region, indicating the point defect densities at the mouth region are higher those at the crack tip region, which is the same as observed for Alloy 690. Such observation could have been related to the oxide film degradation due to the hydrogen uptake. The mouth region was exposed to high temperature water and would absorb more hydrogen generated by corrosion reactions [28]. Higher hydrogen concentration would increase the dissolved interstitial protons in the oxide films and thus increase the defects like metal vacancies and oxygen interstitials [29]. Meanwhile, the crack tip region as the relative “fresh” area would have hydrogen concentration and less point defect.

Although the M-S curves of Alloy 690 and 316 SS show p-n heterojunction semiconductors features, the p-type character is dominant for Alloy 690 and n-type character is dominant for 316 SS. It has been reported [30–32] that the semiconductor properties of

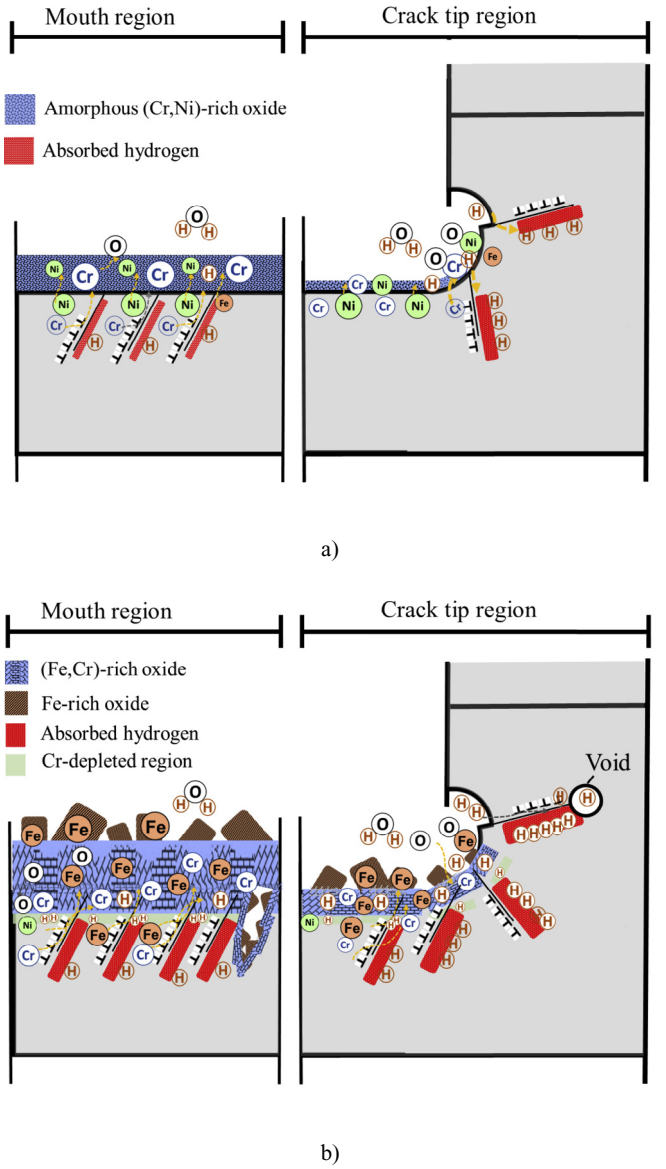

Fig. 10. Schematic illustration of (a) Alloy 690 and (b) 316 SS describing the corrosion mechanisms and fatigue behavior during LCF test in a PWR environment.

oxide films is related to the chemical compositions and structure of oxide films, and the Fe-rich oxide films exhibits n-type behaviors while Cr-rich oxide films p-type behaviors. The TEM results reveal that the oxide films formed on Alloy 690 is Cr enriched and the oxide films on 316 SS is consisted of Fe-rich outer oxide particles and Cr-rich inner layers, as shown in Figs. 4 and 5. The M-S plots are well in accordance with the microstructural analysis.

As shown in Tables 3 and 4, the point defect densities of oxide films formed on Alloy 690 at both the crack tip and mouth region of LCF crack surface are lower than those on 316 SS. Since the defects in the film provide the tunnel for the migration of electron or/and ion, the decrease of point defect densities results in the increase of charge transfer resistance of the oxide film [33]. The higher charge transfer resistances of oxide films of Alloy 690 from EIS results (Fig. 6 and Table 3) are in good agreement with M-S results. It further suggests that the oxide layers on the LCF crack surface of Alloy 690 are less defective than those of 316 SS. According to reports that investigated the effect of hydrogen on the behavior of oxide layers [2,24,25], hydrogen could increase the defect densities of both p-type and n-type semiconductors in the oxide layers. Thus, high defect densities in the oxide layers for 316 SS, in part, could have resulted in more corrosion and more hydrogen generation at the crack tip. In addition, hydrogen can diffuse through the oxide layers to the metal matrix and subsequently induce HIC in a PWR environment [9].

3.5. Corrosion mechanisms and environmental fatigue behavior

The corrosion process on the LCF crack surface and the environmentally-assisted fatigue behavior of Alloy 690 and 316 SS are described schematically in Fig. 10. For Alloy 690, a thin (Cr,Ni)-rich amorphous oxide is formed on the LCF crack surface. For 316 SS, the oxide film is consisted with (Cr,Fe)-rich spinel-type inner oxide film and Fe-rich magnetite outer oxide nodules. Overall, the oxide film is much thicker for 316 SS than for Alloy 690, as shown in Figs. 4 and 5. The ex-situ electrochemical tests demonstrated that the oxide films of Alloy 690 are with lower point defect densities and higher reaction resistance, suggesting that the corrosion rate of Alloy 690 is lower than 316 SS in the case of current study.

It has been reported that the HIC mechanism is dominant in the progress of EAF of SS and Ni-base alloy in simulated PWR primary water environments [5,7–9,34]. HIC was clearly observed as the key cracking mechanism of 316 LN SS in high temperature deoxygenated water during LCF tests, showing some voids near the crack tip area because of the trapped hydrogen [7]. For this mechanism, in the crack tip area, the main anodic reactions are the anodic dissolution of metal and the formation of oxides as follows:

$$M \rightarrow M^{n+} + ne^- \quad (3)$$

$$M^{n+} + pH_2O \rightarrow M(OH)_{+\ p}^{(n-p)} + pH^+ \quad (4)$$

$$2M(OH)_{+\ p}^{(n-p)} + qO_2 + 2(n-p)e^- \rightarrow 2M(O)_{q+p/2} + pH_2O \quad (5)$$

The main cathodic reactions are hydrogen evolution and oxygen reduction:

$$H^+ + e^- \rightarrow H_{abs} \quad (6)$$

$$pO_2 + 2pH_2O + 4pe^- \rightarrow 4pOH^- \quad (7)$$

The hydrogen evolution occurred in the region near the crack tip when the bare metal is exposed due to oxide rupture, the hydrogen would be absorbed into the metal during cyclic loading. The hydrogen evolution rates depend on the corrosion current density of alloys in a PWR primary water environment. The higher corrosion rate of 316 SS during LCF tests would result in the higher cathodic reaction rates of hydrogen evolution and oxygen reduction. Meanwhile, the reported hydrogen diffusion coefficient in 316 SS (1.48×10^{-7} cm^2/s) [35] has no obvious different with Alloy 690 (1.97×10^{-7} cm^2/s) [36] at 310 °C. Also, TEM results shown in Figs. 4a and 5a reveals that the thickness of inner oxide film formed on the fracture surface of 316 SS (30–100 nm) is similar to that of Alloy 690 (50–70 nm). Considering the little difference in the thickness of the inner oxide layer between 316 SS and Alloy 690, the different characteristics of inner oxide layer affecting the hydrogen and oxygen diffusion would play more important roles in the EAF behavior of these alloys.

It has been reported that the oxygen diffusion coefficient in the oxide layers formed on Ni-base alloys is lower than stainless steels [24]. Previously, the transport of hydrogen through the oxide layers has been observed to be faster at the fracture surface oxide layers of 316 SS than Alloy 690 [24,25]. The lower oxygen diffusion in the oxide layers of Alloy 690 would also induce its lower corrosion rate than 316 SS. The lower corrosion rate would further decrease the cathodic hydrogen evolution. It means Alloy 690 would suffer less HIC mechanism during LCF in simulated PWR primary environment. Moreover, a reduction in the fatigue life of 316 SS comparing to Alloy 690 is also associated with strain localization induced by both dynamic strain aging (DSA) and absorbed hydrogen [8,9]. During LCF deformation, the strain-localized site induced by DSA is a preferred trapping site for absorbed hydrogen. The increasing of hydrogen concentrations in these strain-localized sites enhances the strain localization. For 316 SS, the enhanced strain localization caused by the interaction between DSA and absorbed hydrogen would cause an increase in the local stress and growth of fatigue cracks. Therefore, the lower corrosion rate and lower oxygen diffusivity of the oxide layers on the LCF crack surface of Alloy 690 could have resulted in longer LCF life of Alloy 690 than 316 SS in simulated PWR primary environment.

4. Conclusions

Low-cycle fatigue (LCF) tests were performed for Alloy 690 and 316 SS in a simulated pressurized water reactor (PWR) environment. Alloy 690 showed about twice longer LCF life than 316 SS at the test condition of 0.4% amplitude at strain rate of 0.004%/s. To understand the reasons of such differences, oxides formed on the LCF crack surface, at the crack tip and mouth regions, were observed using transmission electron microscope (TEM) with energy dispersive spectroscope (EDS), and electrochemically analyzed using electrochemical impedance spectroscope (EIS) and Mott-Schottky analysis. Based on the tests and analyses, the following conclusions were drawn:

- The oxide layers on Alloy 690 were dominated by continuous (Cr,Ni)-rich oxide, mostly in an amorphous structure. Meanwhile, outer crystalline Fe-rich oxide nodules and inner (Fe,Cr)-rich oxide layer were present on the LCF crack surface for 316 SS.
- Overall, the oxide layer of Alloy 690 was thinner than 316 SS at both the crack tip and mouth regions. Therefore, the thickness of the Cr-rich oxide layer could not be correlated with the LCF life in a simulated PWR environment.
- The higher charge transfer resistances and lower point defect densities of oxide layers of Alloy 690 than 316 SS was observed according to ex-situ EIS and Mott-Schottky analyses, which suggest that the oxide layers on LCF cracks surface of Alloy 690 would be more protective than those of 316 SS.

- The lower corrosion rate and lower oxygen diffusivity of the oxide layers on the LCF crack surface of Alloy 690 would result in longer LCF life of Alloy 690 than 316 SS in a simulated PWR environment.

Acknowledgments

This study was in part supported by the Korea Hydro and Nuclear Power Co., Ltd. as the Proactive Material Aging Management Project. Additional funding was provided by the KUSTAR-KAIST Institute of KAIST and MSIP/NRF (Engineering Research Center No. 2016R1A5A1013919) of MSIP of the Republic of Korea. Financial support for two of the authors was provided by the BK-Plus Program of the MSIP of the Republic of Korea.

References

[1] T. Couvant, Corrosion in pressurized water reactors (PWRs), in: K.L. Murty (Ed.), Materials' Ageing and Degradation in Light Water Reactors, Woodhead Publishing, 2013, pp. 70–80.
[2] T. Allen, J. Busby, M. Meyer, D. Petti, Materials challenges for nuclear systems, Mater. Today 13 (2010) 14–23.
[3] M. Higuchi, K. Sakaguchi, Y. Nomura, A. Hirano, Final proposal of environmental fatigue life correction factor (Fen), in: Codes Stand, vol. 1, ASME, 2007, pp. 111–122.
[4] O. Chopra, G.L. Stevens, Effect of LWR Coolant Environments on the Fatigue Life of Reactor Materials, NUREG/CR-6909 draft Rev.1, 2014.
[5] C. Jang, H. Jang, J.-D. Hong, H. Cho, T.S. Kim, J.-G. Lee, Environmental fatigue of metallic materials in nuclear power plants – a review of Korean test programs, Nucl. Eng. Technol. 45 (2013) 929–940.
[6] U.S. Nuclear Regulatory Commission, Guidelines for Evaluating Fatigue Analyses Incorporating the Life Reduction of Metal Components due to the Effects of the Light-water Reactor Environment for New Reactors, Regulatory Guide 1.207 Draft Rev. 1, 2014.
[7] H. Cho, B.K. Kim, I.S. Kim, C. Jang, D.Y. Jung, Fatigue life and crack growth mechanisms of the type 316LN austenitic stainless steel in 310°c deoxygenated water, J. Nucl. Sci. Technol. 44 (2007) 1007–1014.
[8] H. Cho, B.K. Kim, I.S. Kim, C. Jang, Low cycle fatigue behaviors of type 316LN austenitic stainless steel in 310°C deaerated water–fatigue life and dislocation structure development, Mater. Sci. Eng. 476 (2008) 248–256.
[9] J.D. Hong, J. Lee, C. Jang, T.S. Kim, Low cycle fatigue behavior of alloy 690 in simulated PWR water—effects of dynamic strain aging and hydrogen, Mater. Sci. Eng. 611 (2014) 37–44.
[10] Y.H. Lu, Q.J. Peng, T. Sato, T. Shoji, An ATEM study of oxidation behavior of SCC crack tips in 304L stainless steel in high temperature oxygenated water, J. Nucl. Mater. 347 (2005) 52–68.
[11] T. Terachi, K. Fujii, K. Arioka, Microstructural characterization of SCC crack tip and oxide film for SUS 316 stainless steel in simulated PWR primary water at 320°C, J. Nucl. Sci. Technol. 42 (2005) 225–232.
[12] O.K. Chopra, W.J. Shack, A review of the effects of coolant environments on the fatigue life of LWR structural materials, J. Pressure Vessel Technol. 131 (2009) 21409.
[13] M. Higuchi, K. Sakaguchi, A. Hirano, Y. Nomura, Revised and new proposal of environmental fatigue life correction factor (Fen), in: Codes Stand, vol. 1, ASME, 2006, pp. 93–102.
[14] M. da Cunha Belo, M. Walls, N.E. Hakiki, J. Corset, E. Picquenard, G. Sagon, D. Noël, Composition, structure and properties of the oxide films formed on the stainless steel 316L in a primary type PWR environment, Corrosion Sci. 40 (1998) 447–463.
[15] R. Soulas, M. Cheynet, E. Rauch, T. Neisius, L. Legras, C. Domain, Y. Brechet, TEM investigations of the oxide layers formed on a 316L alloy in simulated PWR environment, J. Mater. Sci. 48 (2013) 2861–2871.
[16] F. Carrette, M.C. Lafont, L. Legras, L. Guinard, B. Pieraggi, Analysis and TEM examinations of corrosion scales grown on alloy 690 exposed to PWR environment, Mater. A. T. High. Temp. 20 (2003) 581–591.
[17] J. Huang, X. Wu, E.-H. Han, Electrochemical properties and growth mechanism of passive films on Alloy 690 in high-temperature alkaline environments, Corrosion Sci. 52 (2010) 3444–3452.
[18] M. Sennour, L. Marchetti, F. Martin, S. Perrin, R. Molins, M. Pijolat, A detailed TEM and SEM study of Ni-base alloys oxide scales formed in primary conditions of pressurized water reactor, J. Nucl. Mater. 402 (2010) 147–156.
[19] H. Lefaix-Jeuland, L. Marchetti, S. Perrin, M. Pijolat, M. Sennour, R. Molins, Oxidation kinetics and mechanisms of Ni-base alloys in pressurised water reactor primary conditions: influence of subsurface defects, Corrosion Sci. 53 (2011) 3914–3922.
[20] B. Beverskog, I. Puigdomenech, Pourbaix diagrams for the ternary system of iron-chromium-nickel, Corrosion 55 (1999) 1077–1087.
[21] L. Marchetti, F. Miserque, S. Perrin, M. Pijolat, XPS study of Ni-base alloys oxide films formed in primary conditions of pressurized water reactor, Surf. Interface Anal. 47 (2015) 632–642.
[22] H. Shin, F. Mansfeld, Concerning the use of the Kramers-Kronig transforms for the validation of impedance data, Corrosion Sci. 28 (1988) 933–938.
[23] Y. Qiu, T. Shoji, Z. Lu, Effect of dissolved hydrogen on the electrochemical behaviour of Alloy 600 in simulated PWR primary water at 290°C, Corrosion Sci. 53 (2011) 1983–1989.
[24] M. Dumerval, S. Perrin, L. Marchetti, M. Tabarant, F. Jomard, Y. Wouters, Hydrogen absorption associated with the corrosion mechanism of 316L stainless steels in primary medium of pressurized water reactor (PWR), Corrosion Sci. 85 (2014) 251–257.
[25] F. Jambon, L. Marchetti, F. Jomard, J. Chêne, Characterisation of oxygen and hydrogen migration through oxide scales formed on nickel-base alloys in PWR primary medium conditions, Solid State Ionics 231 (2013) 69–73.
[26] K. Oh, S. Ahn, K. Eom, H. Kwon, A Study on the localized corrosion and repassivation kinetics of Fe-20Cr- x Ni (x = 0–20 wt%) stainless steels via electrochemical analysis, Corrosion Sci. 100 (2015) 158–168.
[27] J.J. Kim, M.Y. Yu, Study on the passive film of type 316 stainless steel, Int. J. Electrochem. Sci. 8 (2013) 11847–11859.
[28] D.S. Morton, S.A. Attanasio, G.A. Young, P.L. Andresen, T.M. Angeliu, The influence of dissolved hydrogen on Nickel alloy SCC: a window to fundamental insight, in: Corrosion'2001, NACE, 2000, p. 01117.
[29] D. Kim, I. Sah, H.J. Lee, C. Jang, Hydrogen effects on oxidation behaviors of Haynes 230 in high temperature steam environments, Solid State Ionics 243 (2013) 1–7.
[30] C. Sunseri, Photocurrent spectroscopic investigations of passive films on chromium, J. Electrochem. Soc. 137 (1990) 2411.
[31] A. Di Paola, D. Shukla, U. Stimming, Photoelectrochemical study of passive films on stainless steel in neutral solutions, Electrochim. Acta 36 (1991) 345–352.
[32] W.S. Li, J.L. Luo, Uniformity of passive films formed on ferrite and martensite by different inorganic inhibitors, Corrosion Sci. 44 (2002) 1695–1712.
[33] M. Sennour, L. Marchetti, S. Perrin, R. Molins, M. Pijolat, O. Raquet, Characterization of the oxide films formed at the surface of ni-base alloys in pressurized water reactors primary coolant by transmission electron microscopy, Mater. Sci. Forum 595–598 (2008) 539–547.
[34] H. Jang, J.-H. Kim, C. Jang, J.G. Lee, T.S. Kim, Low-cycle fatigue behaviors of two heats of SA508 Gr.1a low alloy steel in 310°C air and deoxygenated water—effects of dynamic strain aging and microstructures, Mater. Sci. Eng. 580 (2013) 41–50.
[35] D.M. Grant, D.L. Cummings, D.A. Blackburn, Hydrogen in 316 steel—diffusion, permeation and surface reaction, J. Nucl. Mater. 152 (1988) 139–145.
[36] M. Uhlemann, B.G. Pound, Diffusivity, solubility and trapping behavior of hydrogen in alloys 600, 690tt and 800, Corrosion Sci. 40 (1998) 645–662.